

Learning Agile Intruder Interception using Differentiable Quadrotor Dynamics

Michael Anoruo^{†,*}, Xiaoyu Tian^{†,*}, Abhishek Rathod[†], Timothy Naudet[§]
 Thomas Canchola[§], Eric Sturzinger[§], Kshitij Goel[†], and Wennie Tabib[†]

[†]Carnegie Mellon University, [§]Artificial Intelligence Integration Center
<http://rislab.github.io/projects/catchrl.html>

Abstract: This paper presents a methodology for learning a control policy to intercept an intruder using the 3D direction unit vector to the intruder and the interceptor state. Prior deep reinforcement learning approaches assume either relative position or distance to the intruder is available, but this information is not readily accessible in real-world applications that employ passive, monocular camera sensors. Instead, we propose a solution that leverages an analytical policy gradient method using differentiable quadrotor dynamics to learn agile interception at speeds up to 10 m/s. The proposed approach outperforms baseline methods that utilize simplified point mass dynamics by an average of 30%.

Keywords: Aerial Robots, Deep Reinforcement Learning, Interception

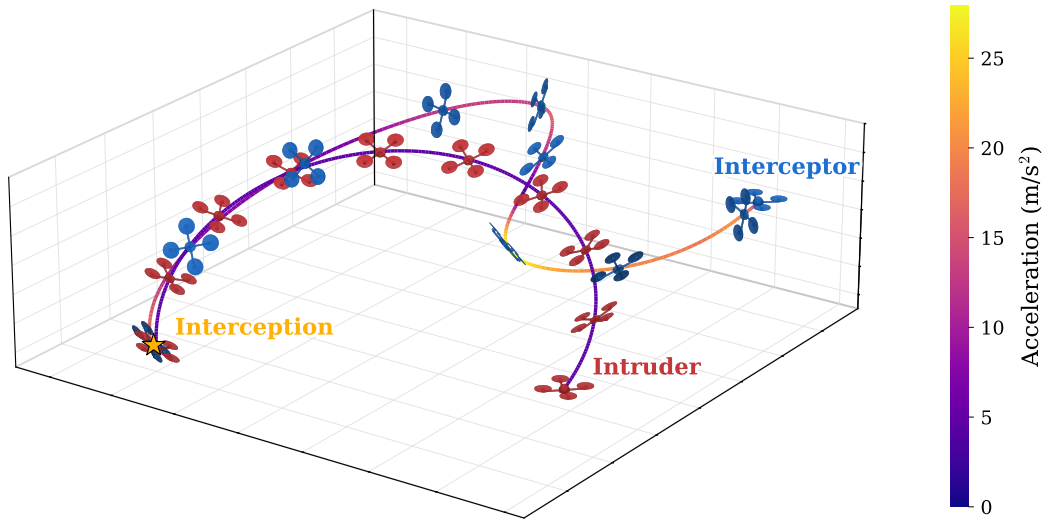


Figure 1: Plot of a rollout in simulation using the proposed control policy. The interceptor (blue) aggressively pursues the intruder (red) flying at 5.8 m/s and collides with it at the star (yellow) labeled interception. The acceleration along the trajectories taken by each agent is plotted from blue (low acceleration) to yellow (high acceleration). Both vehicles are assumed to operate in open air environments in the absence of obstacles.

1 Introduction

Agile unmanned aerial systems have the potential to disrupt airport operations and damage critical urban infrastructure [1]. The ubiquity and low-cost of commercial off-the-shelf unmanned aerial

*Equal contribution.

systems pose challenges for defending restricted airspaces. Thus, the demand for cost-effective countermeasures against unauthorized drone activity is increasing [2]. In this work, we propose a solution that intercepts an intruder drone through forced collisions. Prior works leveraging Deep Reinforcement Learning (DRL) for interception require relative 3D position or distance information during inference for interception; however, this information is not readily available in real-world applications. Instead, we assume the interceptor is equipped with multiple cameras whose images provide 360° coverage. Given this sensing model, object detection is possible on a unit sphere around the interceptor, which determines the direction of the intruder relative to the interceptor.

The problem we address is how to train a policy that uses only the unit direction vector to the intruder and interceptor state as inputs during inference. To this end, we make the following contributions: (1) an end-to-end control policy trained via differentiable simulation for interception; (2) extensive evaluations in simulation that compare the approach against state-of-the-art RL algorithms and multiple dynamics models; and (3) an open source software release¹.

2 Related Work

This section provides an overview of prior work most closely aligned with our approach. These works can be broadly categorized as autonomous interception and learning-based navigation.

Interception: Prior works have leveraged DRL for drone interception [2, 3, 4, 5, 6]; however, these approaches assume that the intruder’s 3D position relative to the interceptor is known during inference, which is challenging to estimate using passive monocular sensing. Our approach assumes that only the 3D direction vector without distance to the intruder is known. In practice, this information could be obtained from an object detector (e.g. YOLO [7]) through a set of onboard cameras.

LiDAR-based intruder detection and interception has been demonstrated in [8, 9], but LiDARs are active sensors that emit pulses of infrared laser light [10], which makes them detectable [11] compared to passive sensors like RGB cameras. LiDARs are also relatively expensive, so methods that leverage passive sensors are preferred. Yan et al. [12], Guo et al. [13] develop visual servoing for intercepting a dynamic intruder, but the approaches are evaluated using simple trajectories that vary the z -altitude exclusively or move along the xy -plane. In contrast, we evaluate our approach with agile 3D trajectories. Liu et al. [14] have proposed using noisy distance observations via a microphone for interception but require two communicating vehicles to intercept one intruder. We propose a strategy that requires one interceptor per intruder.

Prior works have also considered how jamming could be used to interfere with GNSS receivers to intercept drones [15, 16, 17, 18]; however, this is ineffective for systems that can operate in GPS-denied environments (e.g., using visual inertial odometry instead of GPS to navigate). Nets have also been considered to catch rogue drones [19], but multiple systems are required to coordinate to transport the net, which necessitates precise localization using a differential GNSS solution. Further, the solution requires external target detection and tracking [19], which limits real-world deployment.

Learning-based Quadrotor Navigation using Differentiable Physics: Learning-based quadrotor navigation methods using differentiable quadrotor physics models [20, 21, 22] have demonstrated performance gains and improved sample efficiency over imitation learning methods [23]. Zhang et al. [20] contribute a neural policy that processes a depth image and quadrotor state to output acceleration commands. Instead of leveraging a critic network, their method relies on a simplified point mass dynamics model through which gradients can flow during backpropagation. Extensions to this work have been proposed towards improving yaw control [21] and training stability [22]. To the best of our knowledge, differentiable simulation has not been used in prior work to address the interception problem. We address this gap in this paper by developing an end-to-end interception policy trained via differentiable simulation.

¹<https://github.com/rislab/catchrl>

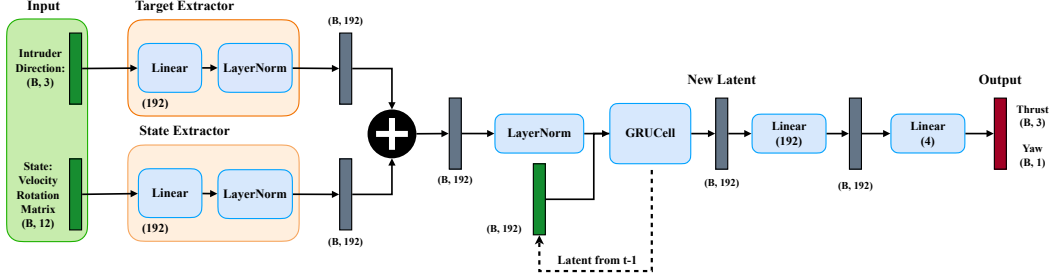


Figure 2: Overview of the network architecture for the interception control policy. The 3D direction vector to the intruder from the interceptor is used as an input to the policy along with the interceptor linear velocity and rotation matrix flattened to a 9-dimensional vector. MLP encoders process the intruder and interceptor data separately to produce 192-dimensional embeddings, which are summed and passed to a GRU with 192 hidden units. The output of the GRU is fed through a single hidden layer before a linear head to generate the interceptor control commands.

3 Methodology

We design a learning-based control policy for a quadrotor agent intercepting a dynamic intruder in an open 3D workspace. The policy (see Fig. 2) receives quadrotor proprioception and a unit direction vector to the intruder. A recurrent neural network (RNN) maps the onboard observations to a 3D thrust and heading command which are used to intercept the intruder.

At time t , let the state of this system be $x_t \in \mathcal{X}$, where \mathcal{X} is the continuous state space for the interceptor and the intruder. The interceptor observes $o_t = [\mathbf{v}_t, \mathbf{R}_t, \hat{\mathbf{d}}_t]$, where $\mathbf{v}_t \in \mathbb{R}^3$ is the interceptor’s linear velocity, $\mathbf{R}_t \in \text{SO}(3)$ is the interceptor body-to-start rotation matrix, and $\hat{\mathbf{d}}_t \in \mathbb{S}^2$ is the unit direction vector to the intruder from the interceptor, expressed in the frame aligned with the starting pose of the interceptor. The policy outputs $u_t = [\mathbf{a}_t^{\text{cmd}}, \psi_t]$ consist of the 3D commanded mass-normalized thrust vector for the interceptor $\mathbf{a}_t^{\text{cmd}} \in \mathbb{R}^3$ and a scalar yaw angle $\psi_t \in \mathbb{R}$. These outputs are tracked using a PD attitude controller [24] onboard the quadrotor interceptor. In general, all the inputs and outputs of the policy are expressed in the start frame.

The policy $u_t = \pi_\theta(o_t)$ is represented using a neural network with θ parameters. We leverage the Analytical Policy Gradient (APG) method [25] which backpropagates gradients through time (BPTT) using a differentiable dynamics model to optimize the network parameters via gradient descent [20]. Formally, we want to find the optimal policy parameters that minimize the loss over a trajectory containing T timesteps, $\theta^* = \arg \min_\theta \sum_{t=0}^T \mathcal{L}(x_t, \pi_\theta(o_t))$, where \mathcal{L} is the per-step loss. To this end, the following sections describe the network architecture for π_θ , the differentiable dynamics model used for APG, and the objective functions that contribute to \mathcal{L} and enable dynamic intruder interception.

3.1 Policy Network Architecture

The policy network is designed to exploit the temporal structure of the interception task while remaining compatible with BPTT-based optimization [20] (see Fig. 2). The proprioceptive state $[\mathbf{v}_t, \mathbf{R}_t]$ and the 3D unit direction vector to the intruder $\hat{\mathbf{d}}_t$ are processed by two separate MLP encoders, each producing a 192-dimensional embedding. The two embeddings are summed and passed to a Gated Recurrent Unit (GRU) with 192 hidden units, whose output is fed through a single hidden layer (192 units) before a linear head emitting the four-dimensional action $[\mathbf{a}_t^{\text{cmd}}, \psi_t]$. The recurrent state enables the policy to integrate information across timesteps, implicitly estimating intruder velocity and acceleration from the temporal sequence of 3D direction measurements. This is essential for predictive interception given that the intruder velocity and absolute position are unobservable during inference.

3.2 Differentiable Dynamics Model

Recent works that leverage APG and BPTT for training a quadrotor navigation policy opt for a simplified point mass dynamics model to enable higher sample efficiency and shorter training times [20, 21]. However, for the dynamic interception task, we found that the nonlinear quadrotor dynamics model provides a higher interception accuracy relative to the point mass approximation.

The quadrotor is modeled as a rigid body with state $[\mathbf{p}, \mathbf{v}, \mathbf{q}, \boldsymbol{\omega}]$ representing position, linear velocity, attitude quaternion, and body-frame angular velocity, respectively. Its dynamics evolve according to

$$\dot{\mathbf{p}} = \mathbf{v}, \quad \dot{\mathbf{v}} = \frac{1}{m} \mathbf{R}_{wb}(\mathbf{f} + \mathbf{d}(\mathbf{v})) - g\hat{\mathbf{z}}, \quad (1)$$

$$\dot{\mathbf{q}} = \frac{1}{2} \mathbf{q} \otimes \boldsymbol{\omega}, \quad \dot{\boldsymbol{\omega}} = \mathbf{J}^{-1}(\boldsymbol{\tau} - \boldsymbol{\omega} \times \mathbf{J}\boldsymbol{\omega}), \quad (2)$$

where \mathbf{R}_{wb} is the body-to-world rotation, $\mathbf{f} = [0, 0, u_1]^\top$ is the collective thrust in the body frame, $\boldsymbol{\tau}$ is the body torque, \mathbf{J} is the inertia matrix, and g is gravity. The aerodynamic drag is modeled as

$$\mathbf{d}(\mathbf{v}) = -k_{d,1} \|\mathbf{v}\| \mathbf{v} - k_{d,2} \mathbf{v}, \quad (3)$$

where $k_{d,1}$ and $k_{d,2}$ are drag coefficients. The collective thrust u_1 and body torque $\boldsymbol{\tau}$ are produced by four rotors. An attitude-rate controller converts the policy’s high-level thrust-and-yaw command into desired rotor speeds $\Omega_{\text{cmd},i}$. To capture real-world latency, the actual rotor speeds Ω_i are modeled with a first-order delay:

$$\dot{\Omega}_i = \frac{1}{\tau_r} (\Omega_{\text{cmd},i} - \Omega_i), \quad (4)$$

where τ_r is the rotor time constant. The forces and torques are then generated via a quadratic thrust model and mixer matrix. The ordinary differential equation above is integrated with the fixed-step 4th order Runge–Kutta (RK4) method. This model is differentiable and can be used within the APG-based policy optimization.

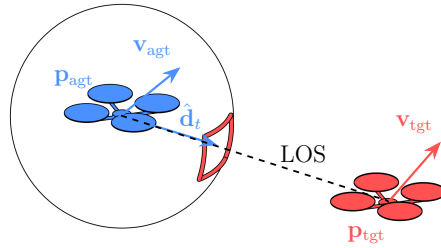
3.3 Objective Functions

The training objective minimizes the weighted sum of the guidance and regularization terms. The total per-step loss is

$$\mathcal{L}_t = \lambda_{\text{align}} \mathcal{L}_{\text{align}} + \lambda_{\text{close}} \mathcal{L}_{\text{close}} + \lambda_{\text{acc}} \mathcal{L}_{\text{acc}} + \lambda_{\text{jerk}} \mathcal{L}_{\text{jerk}} + \lambda_{\text{vmax}} \mathcal{L}_{\text{vmax}} + \lambda_{\text{yaw}} \mathcal{L}_{\text{yaw}}. \quad (5)$$

Each term is described below. We leverage the intruder’s position and velocity as privileged information for loss computation. This information is not provided as an input to the policy during deployment. This setup encourages emergent interception behavior while maintaining realistic observation constraints at inference time. All terms are calculated in the world frame.

Guidance: Inspired by parallel navigation [26], these terms enable intruder interception (see inset figure). Let $\mathbf{d}_t = \mathbf{p}_{\text{tgt}} - \mathbf{p}_{\text{agt}}$ be the relative position and $\mathbf{v}_{\text{rel},t} = \mathbf{v}_{\text{tgt}} - \mathbf{v}_{\text{agt}}$ the relative velocity of the interceptor (agt) and the intruder (tgt). The unit line-of-sight (LOS) vector is $\hat{\mathbf{d}}_t = \mathbf{d}_t / \|\mathbf{d}_t\|$. The parallel-navigation criterion decomposes into two scalar quantities. The first term captures the angular drift of the LOS,



$$m_t = \mathcal{L}_{\text{align}} = \|\hat{\mathbf{d}}_t \times \hat{\mathbf{v}}_{\text{rel},t}\| = \sin \angle(\mathbf{d}_t, \mathbf{v}_{\text{rel},t}), \quad (6)$$

which vanishes when the relative velocity is aligned with the LOS. The second term captures the rate of approach along the LOS,

$$v_{c,t} = -\mathcal{L}_{\text{close}} = -\hat{\mathbf{d}}_t^\top \mathbf{v}_{\text{rel},t}, \quad (7)$$

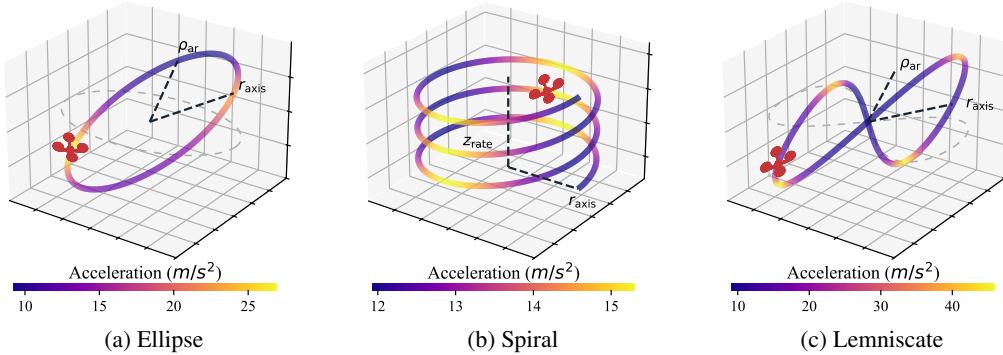


Figure 3: Example (a) ellipse, (b) spiral, and (c) lemniscate intruder trajectories. The ellipse trajectories are used for training while all are used in evaluation. The parameters of the trajectories are randomly sampled (Appendix A.1). A subset of these parameters, r_{axis} , ρ_{ar} , and z_{rate} , are visualized and denote the semi-axis, aspect ratio, and vertical ascent rate for the spiral, respectively. The trajectories are colored according to the magnitude of the acceleration. (a)–(c) present increasingly challenging interception tasks.

which is positive when the gap is shrinking. The policy is trained to *minimize* m_t and *maximize* $v_{c,t}$. The alignment term penalizes the sine of the angle between the relative position and relative velocity vectors, vanishing when the agent moves along the LOS to the intruder. The closing term (note the sign — minimizing the loss *maximizes* closing speed) drives the agent to shrink the gap rather than pointing to the intruder.

Regularization: To produce smooth trajectories, we penalize commanded acceleration, jerk, and speed:

$$\mathcal{L}_{\text{acc}} = \|\mathbf{a}_t\|^2, \quad \mathcal{L}_{\text{jerk}} = \|\mathbf{j}_t\|^2, \quad \mathcal{L}_{\text{vmax}} = \max(0, \|\mathbf{v}_t\| - v_{\text{des}})^2. \quad (8)$$

The acceleration penalty discourages excessive control effort; the jerk penalty enforces temporal smoothness, mitigating high-frequency oscillations that destabilize BPTT; and the one-sided velocity penalty keeps trajectories within the platform’s flight envelope while leaving the agent free to operate below the desired speed v_{des} .

Yaw Alignment: We add a loss term that helps the policy align the body x -axis with the intruder direction:

$$\mathcal{L}_{\text{yaw}} = -\hat{\mathbf{d}}_t^\top \hat{\mathbf{b}}_{1,t}, \quad (9)$$

where $\hat{\mathbf{b}}_{1,t}$ is the world-frame projection of the body x -axis onto the horizontal xy -plane.

4 Results

Experimental Design: Our method is evaluated using a custom-built parallelized, GPU-accelerated simulator written in PyTorch [27]. The intruder is successfully intercepted if its position is within a capture radius c_r at any time. If after T_{ep} timesteps or when the distance between the intruder and interceptor exceeds the escape radius e_r , the interception is considered to have failed. Each timestep is Δt_{ctrl} seconds long. The success rate is measured as the number of rollouts that terminate in success divided by the total number of rollouts. For each rollout, the interceptor’s initial position and orientation are randomized within a box of side length s_{box} , and the intruder is initialized on a sampled trajectory. All evaluation rollouts utilize the nonlinear quadratic dynamics model. We sweep loss coefficients of our approach as detailed in Section A.2. The values for all parameters are provided in Section A.4.

The sampled trajectories consist of three types: ellipse, spiral, and lemniscate (see Fig. 3). Ellipse trajectories are used for both training and evaluation, whereas the lemniscate and spiral trajectories

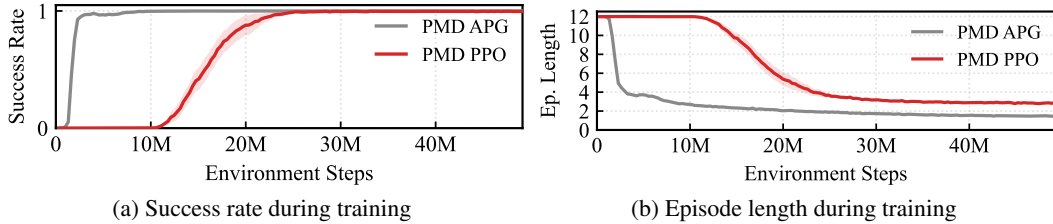


Figure 4: Training success rate and episode length variation with environment steps demonstrate that APG is more sample-efficient than PPO.

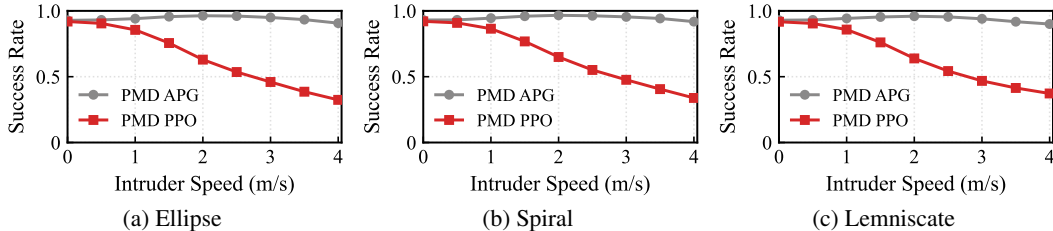


Figure 5: The success rates obtained while varying intruder speeds during evaluation demonstrate that using APG enables a higher interception accuracy than PPO for all three types of intruder trajectories.

are used only for evaluation. The ellipse trajectories used during training expose the interceptor to a wide range of maneuvers to intercept the intruder. The lemniscate and spiral trajectories evaluate the generalizability of the approach to more complex motions. Each trajectory is generated by randomly sampling parameters (see Appendix A.1), including a constant speed for the intruder to follow and geometric parameters such as the major axis, aspect ratio, orientation, and ascent rate.

Implementation Details: During both training and evaluation, rollouts that terminate early due to either successful interception or exceeding environment bounds, are frozen until all parallel rollouts complete execution to synchronously update the policy parameters. Experiments were conducted on an NVIDIA RTX 5090 GPU. Unless otherwise specified, policies were trained for 1500 updates using a horizon length of 64 steps across 512 parallel environments, corresponding to approximately 49.15 million steps. We evaluate the learnt policies in 110,000 environments.

Evaluation of APG and PPO using Point Mass Dynamics (PMD): Prior works [20, 21] have leveraged simplified point mass dynamics and differentiable physics for quadrotor navigation tasks due to their computational efficiency. Given this prior work, we conduct an analysis to evaluate the performance of APG using a simplified point mass dynamics model and compare its performance against the state-of-the-art model-free baseline PPO [28]. Consistent with prior work, we employ domain randomization (see Table 5) to help the PMD policies generalize to the quadrotor dynamics.

The baseline PPO policy is implemented using GAE [29] and two separate networks for the actor and critic. The actor and critic networks leverage the same architecture used in our proposed method (the parameters used for PPO training may be found in Table 3). For a fair comparison, both policies share the same state and action space, and are trained against the same objective function in Eq. (5). The interceptor is initialized in a stable hover state at the beginning of each episode.

To analyze the performance, we generate two sets of plots. First, we provide a mean and standard error plot (Fig. 4) for success rate and episode length observed during training for both approaches based on 10 training runs with different random number generator seeds. The second set of plots (Fig. 5) evaluates the generalizability of each approach across different trajectories and velocity profiles of the intruder. We find that APG is more sample-efficient than PPO (Fig. 4a), which is consistent with prior work [20]. Figure 4b shows that PPO takes longer to intercept the intruder. Figure 5 shows the success rates for the ellipse, spiral, and lemniscate trajectories. The PMD APG

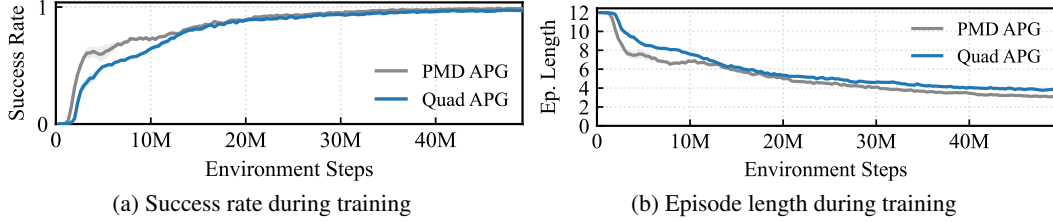


Figure 6: Training success rate and episode length variation with environment steps show a similar rate of convergence when simplified point mass dynamics and nonlinear quadrotor dynamics models are used with APG.

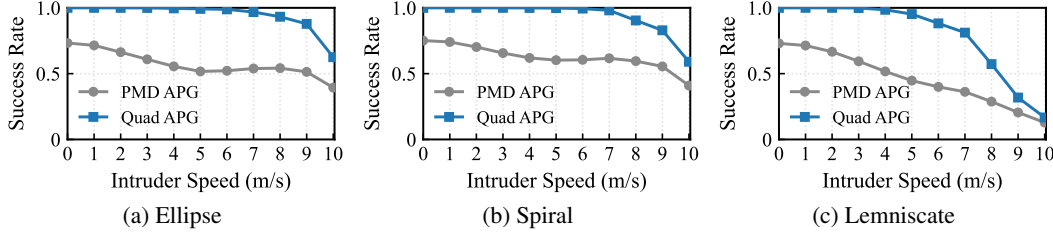


Figure 7: The success rates obtained while varying intruder speeds during evaluation demonstrate that using the nonlinear quadrotor dynamics model enables a higher interception accuracy compared to using simplified point mass dynamics for all three types of intruder trajectories.

approach consistently outperforms the PMD PPO approach and widens the success gap as the speed of the intruder is increased.

These analyses assume a relatively large platform (i.e., 2.65 kg) with a thrust-to-weight ratio of 2.7, which affects the agility of the platform and causes motor saturation at high intruder speeds beyond 4 m/s. The PMD and Quad interceptor platform parameters are provided in Table 5 and Table 6, respectively.

Evaluation of PMD APG Compared to APG Trained with Quadrotor Dynamics: While prior works [20, 21] have shown that simplified point mass dynamics are sufficient for quadrotor navigation, the navigation problem seeks to achieve a single setpoint. The interception problem is fundamentally different as it requires more agile maneuvers to catch a high-speed moving intruder. For this reason, we opt for using the nonlinear quadrotor dynamics model.

For these experiments, we reduce the interceptor mass to 1 kg effectively increasing the thrust-to-weight ratio and platform agility of the interceptor. In the next section, we provide results to quantify the performance for a larger and higher range of intruder speeds with a more agile interceptor. Given the superior performance of PMD APG compared to PMD PPO, we compare PMD APG against APG trained using quadrotor dynamics (Quad APG).

To evaluate the performance of PMD APG and Quad APG, we provide two sets of plots. The first set evaluates the training performance (see Fig. 6). We observe PMD and Quad dynamics models require a similar number of environment steps for convergence. During evaluation, which is shown in Fig. 7, we see that the success rate for the Quad APG policy is substantially higher compared to the PMD APG policy. The Quad APG policy is able to intercept approximately 60% of intruders at speeds up to 8 m/s (compared to approximately 30% of intruders for PMD APG). For each of the ellipse, spiral, and lemniscate evaluation trajectories, the Quad APG policy outperforms the PMD APG policy on average by 37%, 33%, and 31%, respectively. Figure 8 provides qualitative examples of rollouts for the Quad APG policy using the three trajectory types.

Training Times: The Quad APG policy takes approximately 137 minutes, the PMD APG policy takes 10 minutes, and PMD PPO takes approximately 7 minutes. Though significantly faster to

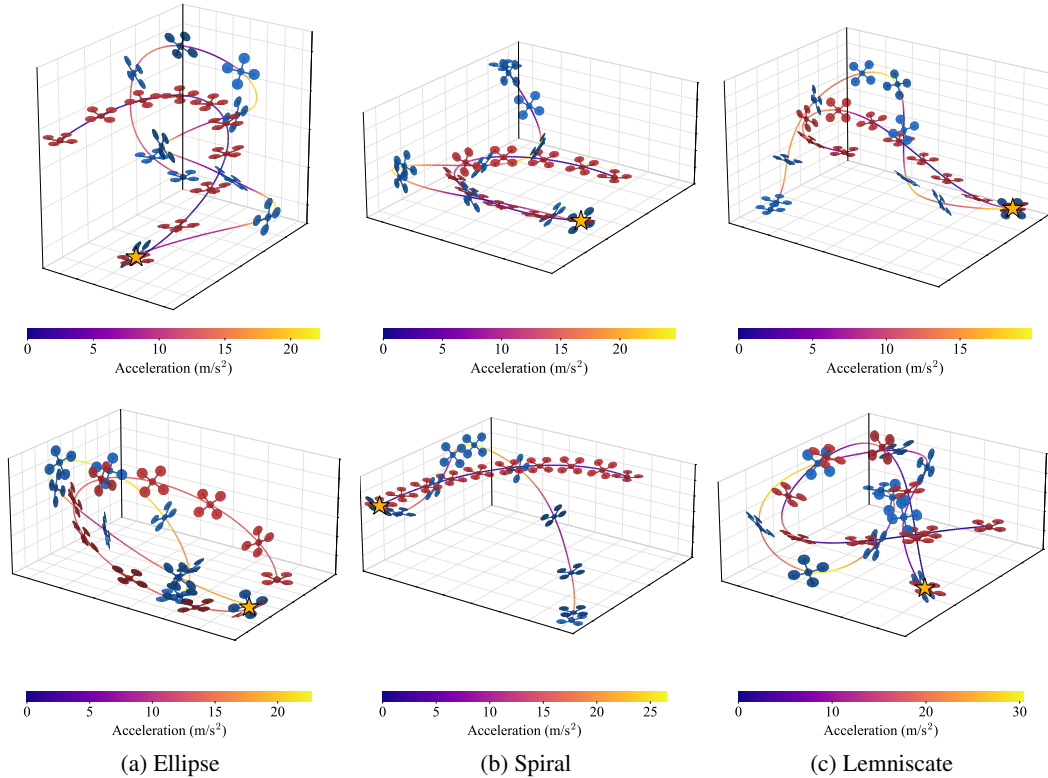


Figure 8: Example rollouts with acceleration heatmaps of the proposed Quad APG policy. Collision between the intruder (red) and the interceptor (blue) occurs at the point marked with a star.

train, the low fidelity of the point mass model means it cannot capture the full range of rigid-body dynamics that a true quadrotor model exhibits.

5 Conclusion

This paper presented a methodology to intercept an intruder by learning agile maneuvers using differentiable simulation. The interceptor state and 3D unit direction vector to the intruder are provided as inputs to the policy to infer the high-level control commands for interception. The policy parameters are optimized using the sample-efficient analytical policy gradients. Training through the quadrotor dynamics instead of simplified point mass dynamics yields higher interception rates ($\geq 30\%$ on average) for a wide range of intruder speeds (up to 10 m/s).

Limitations: The current approach assumes that the intruder uses a constant speed to execute the trajectory; however, this is not representative of an adversarial scenario. Future work includes developing a policy that intercepts adversarial evaders. Our approach also assumes that the intruder is always within the field of view of the interceptor and does not incorporate sensor or detection uncertainty. Hardware validation also remains an area of future work.

Acknowledgments

This research was supported in part by an AI2C Seed grant and the NVIDIA Academic Grant Program.

References

- [1] A. N. Skraparlis, K. S. Ntalianis, and N. Tsapatsoulis. A novel framework to intercept gps-denied, bomb-carrying, non-military, kamikaze drones: Towards protecting critical infrastructures. *Defence Technology*, 40:225–241, 2024. ISSN 2214-9147. doi:<https://doi.org/10.1016/j.dt.2024.05.001>. URL <https://www.sciencedirect.com/science/article/pii/S2214914724001089>.
- [2] T. Gavin, S. Lacroix, and M. Bronz. Agile interception of a flying target using competitive reinforcement learning, 2026. URL <https://arxiv.org/abs/2603.16279>.
- [3] A. S. Roncero, Y. Cai, O. Andersson, and P. Ogren. Learned controllers for agile quadrotors in pursuit-evasion games. 2026. URL <https://arxiv.org/abs/2506.02849>.
- [4] C. Zheng, Z. Guo, Z. Yin, C. Wang, Z. Wang, and S. Zhao. Non-equilibrium mav-capture-mav via time-optimal planning and reinforcement learning, 2026. URL <https://arxiv.org/abs/2503.06578>.
- [5] J.-E. Pierre, X. Sun, and R. Fierro. Multi-agent partial observable safe reinforcement learning for counter uncrewed aerial systems. *IEEE Access*, 11:78192–78206, 2023. doi:10.1109/ACCESS.2023.3298601.
- [6] R. Logiewa, F. Hoffmann, F. Govaers, and W. Koch. Dynamic pursuit-evasion scenarios with a varying number of pursuers using deep sets. In *2023 IEEE Symposium Sensor Data Fusion and International Conference on Multisensor Fusion and Integration (SDF-MFI)*, pages 1–7, 2023. doi:10.1109/SDF-MFI59545.2023.10361514.
- [7] J. Redmon, S. Divvala, R. Girshick, and A. Farhadi. You only look once: Unified, real-time object detection. In *2016 IEEE Conference on Computer Vision and Pattern Recognition (CVPR)*, pages 779–788, 2016. doi:10.1109/CVPR.2016.91.
- [8] M. Pliska, M. Vrba, T. Báča, and M. Saska. Towards safe mid-air drone interception: Strategies for tracking and capture. *IEEE Robotics and Automation Letters*, 9(10):8810–8817, 2024. doi:10.1109/LRA.2024.3451768.
- [9] M. Vrba, V. Walter, V. Pritzl, M. Pliska, T. Báča, V. Spurný, D. Heřt, and M. Saska. On onboard lidar-based flying object detection. *IEEE Transactions on Robotics*, 41:593–611, 2025. doi:10.1109/TRO.2024.3502494.
- [10] J. Ryde and N. Hillier. Performance of laser and radar ranging devices in adverse environmental conditions. *Journal of Field Robotics*, 26(9):712–727, 2009. doi:<https://doi.org/10.1002/rob.20310>. URL <https://onlinelibrary.wiley.com/doi/abs/10.1002/rob.20310>.
- [11] M. Zygmunt and K. Kopczyński. Laser warning system as an element of optoelectronic battlefield surveillance. In P. Kaniewski and J. Matuszewski, editors, *Radioelectronic Systems Conference 2019*, volume 11442, page 1144202. International Society for Optics and Photonics, SPIE, 2020. doi:10.1117/12.2565139. URL <https://doi.org/10.1117/12.2565139>.
- [12] H. Yan, K. Yang, Y. Cheng, Z. Wang, and D. Li. Precise interception flight targets by image-based visual servoing of multicopter. *IEEE Transactions on Industrial Electronics*, 72(11):11499–11509, 2025. doi:10.1109/TIE.2025.3559951.
- [13] H. Guo, T. Song, and J. Ye. Dynamic interception image-based visual servoing under gust interference and model uncertainty. In P. of Acta Aero et Astro Sinica, editor, *Proceedings of the 2nd Aerospace Frontiers Conference (AFC 2025)*, pages 410–420, Singapore, 2026. Springer Nature Singapore. ISBN 978-981-95-3037-3. doi:10.1007/978-981-95-3037-3_28.

- [14] F. Liu, S. Yuan, T.-M. Nguyen, and R. Su. Autonomous 3d moving target encirclement and interception with range measurement. In *2025 IEEE/RSJ International Conference on Intelligent Robots and Systems (IROS)*, pages 4581–4588, 2025. doi:10.1109/IROS60139.2025.11246819.
- [15] N. Souli, P. Kolios, and G. Ellinas. Multi-agent system for rogue drone interception. *IEEE Robotics and Automation Letters*, 8(4):2221–2228, 2023. doi:10.1109/LRA.2023.3245412.
- [16] P. Valianti, K. Malialis, P. Kolios, and G. Ellinas. Cooperative multi-agent jamming of multiple rogue drones using reinforcement learning. *IEEE Transactions on Mobile Computing*, 23(12):12345–12359, 2024. doi:10.1109/TMC.2024.3409050.
- [17] X. Ma and M. Gao. “lure the enemy in deep”: Confronting rogue uav through diverse hybrid jamming. *IEEE Access*, 13:68351–68369, 2025. doi:10.1109/ACCESS.2025.3559659.
- [18] N. Souli, P. Kolios, and G. Ellinas. An enhanced autonomous counter-drone system with jamming and relative positioning capabilities. *Robotics and Autonomous Systems*, 194:105160, 2025. ISSN 0921-8890. doi:https://doi.org/10.1016/j.robot.2025.105160. URL https://www.sciencedirect.com/science/article/pii/S092188902500257X.
- [19] J. Rothe, M. Strohmeier, and S. Montenegro. Autonomous multi-uav net defense system for aerial drone interception. In *2025 10th International Conference on Control and Robotics Engineering (ICCRE)*, pages 171–177, 2025. doi:10.1109/ICCRE65455.2025.11093305.
- [20] Y. Zhang, Y. Hu, Y. Song, D. Zou, and W. Lin. Learning vision-based agile flight via differentiable physics. *Nature Machine Intelligence*, 7(6):954–966, 2025. ISSN 2522-5839. doi:10.1038/s42256-025-01048-0. URL http://dx.doi.org/10.1038/s42256-025-01048-0.
- [21] J. Lee, A. Rathod, K. Goel, J. Stecklein, and W. Tabib. Quadrotor navigation using reinforcement learning with privileged information, 2025. URL https://arxiv.org/abs/2509.08177.
- [22] F. Li, S. Wang, Y. Huang, F. Sun, S. Wu, Y. Yan, D. Zou, and W. Yu. Simple but stable, fast and safe: Achieve end-to-end control by high-fidelity differentiable simulation. 2026. URL https://arxiv.org/abs/2604.10548.
- [23] A. Loquercio, E. Kaufmann, R. Ranftl, M. Müller, V. Koltun, and D. Scaramuzza. Learning high-speed flight in the wild. *Science Robotics*, 6(59):eabg5810, 2021. doi:10.1126/scirobotics.abg5810. URL https://www.science.org/doi/abs/10.1126/scirobotics.abg5810.
- [24] D. Mellinger, N. Michael, and V. Kumar. Trajectory generation and control for precise aggressive maneuvers with quadrotors. *The International Journal of Robotics Research*, 31(5):664–674, 2012. doi:10.1177/0278364911434236. URL https://doi.org/10.1177/0278364911434236.
- [25] N. Wiedemann, V. Wüest, A. Loquercio, M. Müller, D. Floreano, and D. Scaramuzza. Training efficient controllers via analytic policy gradient, 2023. URL https://arxiv.org/abs/2209.13052.
- [26] L. C. Yuan. Homing and navigational courses of automatic target-seeking devices. *Journal of Applied Physics*, 19(12):1122–1128, 12 1948. ISSN 0021-8979. doi:10.1063/1.1715028. URL https://doi.org/10.1063/1.1715028.
- [27] A. Paszke, S. Gross, F. Massa, A. Lerer, J. Bradbury, G. Chanan, T. Killeen, Z. Lin, N. Gimelshein, L. Antiga, A. Desmaison, A. Köpf, E. Yang, Z. DeVito, M. Raison, A. Tejani, S. Chilamkurthy, B. Steiner, L. Fang, J. Bai, and S. Chintala. Pytorch: An imperative style, high-performance deep learning library, 2019. URL https://arxiv.org/abs/1912.01703.

- [28] J. Schulman, F. Wolski, P. Dhariwal, A. Radford, and O. Klimov. Proximal policy optimization algorithms. 2017. URL <https://arxiv.org/abs/1707.06347>.
- [29] J. Schulman, P. Moritz, S. Levine, M. Jordan, and P. Abbeel. High-dimensional continuous control using generalized advantage estimation, 2015. URL <https://arxiv.org/abs/1506.02438>.

A Appendix

A.1 Parametric Intruder Trajectories

Table 1: Intruder trajectory families. r_{axis} = semi-axis, ρ_{ar} = axis ratio, z_{rate} = spiral climb per radian.

Family	In-plane $\mathbf{h}(s)$	Vertical $z(s)$	Tilt \mathbf{R}_{tilt}
Ellipse	$(r_{\text{axis}} \cos s, r_{\text{axis}} \rho_{\text{ar}} \sin s, 0)$	0	per-env (ϕ, θ)
Spiral	$(r_{\text{axis}} \cos s, r_{\text{axis}} \rho_{\text{ar}} \sin s, 0)$	$z_{\text{rate}} s$	identity (flat baseline)
Lemniscate	$(r_{\text{axis}} \cos s, \frac{r_{\text{axis}} \rho_{\text{ar}}}{2} \sin 2s, 0)$	0	per-env (ϕ, θ)

Each intruder trajectory is a 3D curve parameterized by a scalar phase s ,

$$\mathbf{p}(s) = \mathbf{c}_0 + \mathbf{R}_{\text{tilt}} \mathbf{h}(s) + z(s) \hat{\mathbf{z}}, \quad (10)$$

where \mathbf{c}_0 is the curve center, $\mathbf{h}(s)$ is an in-plane curve in the xy -plane, and $z(s)$ is a vertical component along the world $\hat{\mathbf{z}}$ axis.

We instantiate three families of trajectories: ellipse, spiral, and lemniscate (Table 1). The tilt \mathbf{R}_{tilt} is a per-rollout ZYX-Euler rotation $\mathbf{R}_{\text{tilt}} = R_z(\psi) R_y(\theta) R_x(\phi)$ that lifts the planar curve into 3D. During training, we use constant speed 3D elliptical trajectories without a dynamic feasibility check. For evaluation, we use all three trajectory types but with an upper bound on maximum acceleration. In the following, $\dot{(\)}$ and $(\)'$ denote derivatives with respect to time and phase, respectively.

A.1.1 Training

Let the desired intruder speed be v_{tgt} . We ensure that the elliptical realization of the parametric curve in Eq. (10) follows this target speed by setting $\dot{s} = v_{\text{tgt}} / \|\mathbf{c}(s)\|$ in $\dot{\mathbf{p}} = \mathbf{c}(s) \dot{s}$, where $\mathbf{c}(s) = \mathbf{R}_{\text{tilt}} \mathbf{h}'(s) + z'(s) \hat{\mathbf{z}}$. The sign of v_{tgt} determines the intruder's direction of traversing the curve.

A.1.2 Evaluation

To impose an upper bound on acceleration, we derive a feasibility predicate directly from the quadrotor model so the evaluation set of trajectories is realizable. The quadrotor produces net world-frame acceleration

$$\mathbf{a}_{\text{net}} = \frac{T_c}{m} \mathbf{b} - g \hat{\mathbf{z}}, \quad (11)$$

where \mathbf{b} is the body thrust axis and T_c the collective thrust. To realize a demanded acceleration \mathbf{a}_d , the rotors must produce the thrust acceleration $\mathbf{a}_t^{\text{cmd}} = \mathbf{a}_d + g \hat{\mathbf{z}}$. This is feasible if

$$\|\mathbf{a}_t^{\text{cmd}}\| \leq A_{\text{max}} \quad \text{and} \quad a_{t,z}^{\text{cmd}} \geq 0, \quad (12)$$

where A_{max} is a maximum acceleration chosen using the maximum RPM values of the four rotors ($N_m = 4$) and a degradation factor η to account for motor time constant, control bandwidth, and error-correction margin. Formally,

$$A_{\text{max}} = \eta \frac{N_m F_m}{m} \quad (13)$$

such that $F_m = f_2 \Omega_{\text{max}}^2 + f_1 \Omega_{\text{max}} + f_0$ is the maximum available per-rotor force and $\eta = 0.6$.

A trajectory represented by the family in Eq. (10) is feasible if every point on the curve satisfies Eq. (12). For the elliptical and lemniscate trajectories, we use a dense grid of phase values s and ensure

$$\max_s \|\mathbf{a}(s) + g \hat{\mathbf{z}}\| \leq A_{\text{max}} \quad \text{and} \quad \min_s a_z(s) \geq -\beta g, \quad (14)$$

where the downward-acceleration fraction $\beta = 0.6$ leaves margin so the attitude controller does not saturate on the descending arc of a tilted orbit. The expression for $\mathbf{a}(s)$ can be derived from Eq. (10)

as

$$\mathbf{a}(s) = v_{\text{tgt}}^2 \left[\frac{\mathbf{c}'(s)}{\|\mathbf{c}(s)\|^2} - \mathbf{c}(s) \frac{\mathbf{c}(s) \cdot \mathbf{c}'(s)}{\|\mathbf{c}(s)\|^4} \right]. \quad (15)$$

The value $a_z(s)$ in Eq. (14) is the z -component of Eq. (15). On the other hand, for the spiral trajectory, we impose $v_{\text{tgt}}^2 \kappa_{\text{max}} \leq mg$, where $\kappa_{\text{max}} = \max_s \kappa(s)$ is the peak in-plane curvature, which is derived from Eq. (10) as $\kappa(s) = \|\mathbf{c}(s) \times \mathbf{c}'(s)\| / \|\mathbf{c}(s)\|^3$.

We use the following algorithm to generate a desired number of these trajectories for different speed magnitudes.

Algorithm 1 Generating a pool of feasible trajectories for a range of speed magnitudes

Require: speed magnitudes, desired number of trajectories, shape-parameter ranges, feasibility test, pool size, draw budget

- 1: **for** each speed magnitude **do**
- 2: $\text{feasible pool} \leftarrow \text{empty}$
- 3: $\text{draws} \leftarrow 0$
- 4: **while** $\text{feasible pool} < \text{pool size}$ **and** $\text{draws} < \text{draw budget}$ **do**
- 5: draw shape parameters uniformly from the ranges \triangleright semi-axis, axis ratio, tilt, z_{rate}
- 6: $\text{draws} \leftarrow \text{draws} + 1$
- 7: **if** the shape is dynamically feasible at this speed **then** \triangleright feasibility test
- 8: add the shape to the *feasible pool*
- 9: **end if**
- 10: **end while**
- 11: **if** $\text{size}(\text{feasible pool}) < \text{desired number of trajectories}$ **then**
- 12: **abort:** feasible region too thin \triangleright widen the ranges or lower the top speed
- 13: **end if**
- 14: $\text{kept} \leftarrow$ farthest-point selection from the *feasible pool* \triangleright max-min in normalized parameter space
- 15: signed-split: assign traversal direction
- 16: output each *kept* shape and its signed speed
- 17: **end for**

The algorithm has three stages. First, *rejection sampling* draws shape parameters uniformly and keeps those that pass the feasibility test, building a pool up to a specified pool size. Second, *farthest-point selection* greedily selects the requested number of pool members that maximize the minimum pairwise distance in normalized parameter space, so the *kept* set is geometrically diverse rather than clumped by feasible-region density. Third, *signed split* assigns a positive direction to half and a negative direction to the other half (reverse traversal) pool of trajectories. Each generation run reports acceptance rate and diversity diagnostics (e.g., closest-pair spread, per-axis coverage, etc.) and aborts if any (family, speed) bucket cannot be filled, so a thin feasible region cannot silently degrade the evaluation trajectory set.

A.2 Hyperparameter Sweeping

A.2.1 Loss Coefficients

For the loss coefficients, λ_{align} , λ_{close} , λ_{acc} , λ_{jerk} , λ_{vmax} , and λ_{yaw} in Eq. (5), we set up hyperparameter sweeping as follows.

Scale: The objective is nearly invariant to a global rescaling $\lambda \rightarrow \alpha\lambda$ absorbed into the policy step size: only the ratios of the weights matter. We anchor $\lambda_{\text{align}}\mathcal{L} = 5$ and search for the remaining weights and the learning rate relative to the anchor.

Trial Objectives: Each trial trains a policy from scratch on the point mass dynamics under a candidate λ , then evaluates it on the high-fidelity quadrotor model. This weight vector is used for all training runs in this paper. The objective is to minimize the scalar

$$J = 300(1 - \text{SR}) + L_{p99}, \quad (16)$$

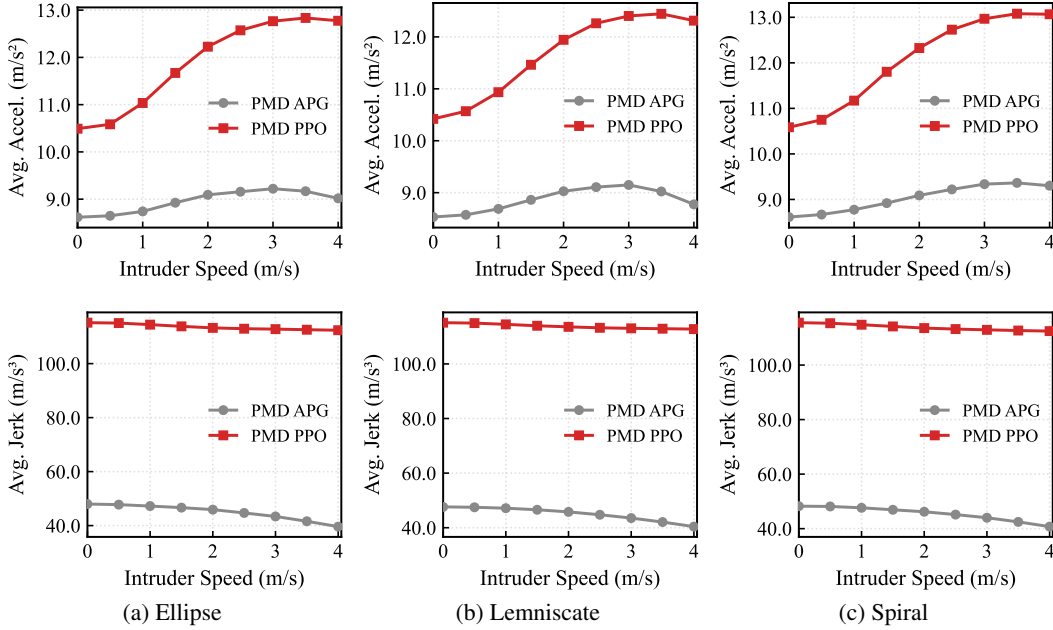


Figure 9: Average acceleration (top row) and jerk (bottom row) across intruder speeds for successful rollouts using APG and PPO. We observe that using the PPO-trained policy leads to higher acceleration and jerk for the interceptor compared to APG.

where $SR \in [0, 1]$ is the interception success rate over the evaluation episodes and L_{p99} is the 99th-percentile episode length (time-to-intercept). Interceptions that take more than 12 seconds are considered failures. The main reason for introducing time-to-intercept into the objective is to break ties between policies with similar success rates, which is common in the high-success regime. The large weight on the success rate ensures that the optimizer prioritizes improving the success rate until it is close to 100%, at which point it will focus on reducing time-to-intercept. This design encourages the discovery of policies that not only succeed but also do so efficiently, rather than optimizing for speed at the expense of reliability. Specifically, 99th-percentile time-to-intercept is used instead of the mean or median to focus on improving the worst-case performance, which is critical for real-world applications where consistent performance is often more important than average performance.

Search procedure: We use Optuna’s TPE sampler via Hydra’s Optuna sweeper plugin². We run it in multivariate mode with an initial 16 random startup trials before the model engages. We run a total of 64 trials per study. All positive weights and the learning rate are given log-uniform priors (they span orders of magnitude); bounded ratios such as the learning-rate decay are also log-uniform.

Iterative range refinement: We first manually adjust the hyperparameters to a suboptimal set that achieves a baseline level of performance showing convergence. We then run a sweep over a wide range around the empirically tested weight sets. However, many trials will be spent in regions of the weight space that are suboptimal or even detrimental to learning. To address this, we run a sequence of studies, after each of which we re-compute the weight set. After every study we compute, per weight: (i) FANOVA and mean-decrease-impurity, (ii) the Spearman rank correlation between the log-weight and J which is a monotonicity measure, (iii) a summary of the top-10% trials, and (iv) the 1D slice plot of J against each weight. Using the shape of the 1D slice, we adjust the next weight set.

²https://hydra.cc/docs/plugins/optuna_sweeper/

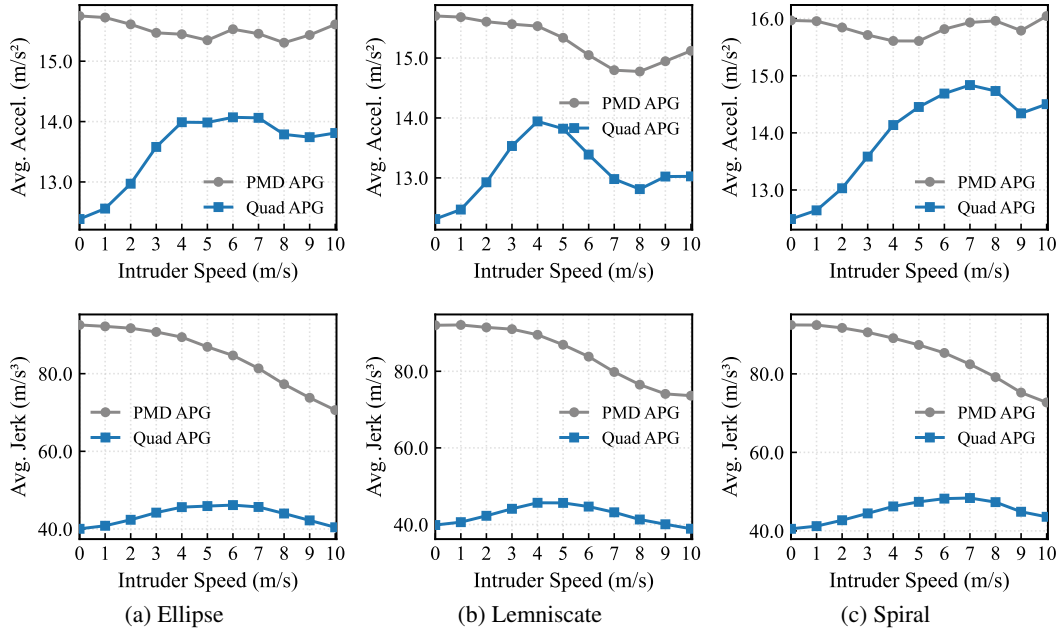


Figure 10: Average acceleration (top row) and jerk (bottom row) across intruder speeds for successful rollouts using the simplified point mass (PMD) and nonlinear quadrotor dynamics (Quad) models with APG. Leveraging the Quad dynamics model provides interception with lower control effort than the PMD case.

A.3 Additional Performance Analysis

In addition to the interception success rate and episode length, we characterize the behavior of the policies by analyzing their acceleration and jerk profiles. We calculated these values for: algorithm comparison (APG vs. PPO) and training dynamics (full quadrotor vs. PMD), and report per-step acceleration and jerk conditioned on the intruder speed.

Policies that produce large acceleration commands tend to behave more aggressively when pursuing the intruder. While aggressive acceleration commands can sometimes help with interception performance, they may also lead to catastrophic overshooting when tracking agile trajectories. Overshooting can leave the policy in undesirable states that are difficult to recover from. Recovering from these scenarios often requires abrupt corrective actions, resulting in increased jerk and higher overall control effort. In our analysis, we study how the acceleration and jerk characteristics learned by a policy correlate with interception success across different trajectory classes.

We first compare the acceleration and jerk profiles of APG and PPO, both trained using simplified point mass dynamics and evaluated on the nonlinear quadrotor dynamics model (see Fig. 9). Similarly, to further understand the performance differences between APG policies trained with these dynamics models, we compare their acceleration and jerk profiles in Fig. 10. For both analyses, we report results only for episodes that terminate with a successful interception of the intruder. In both cases we observe a lower control effort required by the interceptor when APG and nonlinear quadrotor dynamics are used for training.

A.4 Parameters

The experimental configuration is summarized in Tables 2 to 6.

Table 2 reports the settings used for both the algorithm benchmark (PMD PPO vs. PMD APG) and the dynamics benchmark (PMD APG vs. Quad APG). In all experiments, $N_{\text{env}} = 512$ parallel environments were trained for $N_{\text{upd}} = 1500$ updates, with episode capped at $T_{\text{ep}} = 600$ steps.

Table 2: Shared across both benchmarks: training setup (left) and loss-signal weights (right).

Training setup		Signal weight	
	Value		Value
Environments $[N_{\text{env}}]$	512	λ_{align}	5.0
Updates $[N_{\text{upd}}]$	1500	λ_{closing}	1.07
Max episode steps $[T_{\text{ep}}]$	600	λ_{acc}	0.0015
Seeds $[N_{\text{seed}}]$	10	λ_{jerk}	1.96×10^{-4}
Capture radius $[c_r]$ (m)	0.3	λ_{vmax}	0.4
Escape radius $[e_r]$ (m)	100.0	λ_{yaw}	0.064
Spawning box size $[s_{\text{box}}]$ (m)	10.0		

Table 3: Algorithm hyperparameters. Dashes indicate the entry is not applicable to that algorithm.

Parameter	APG	PPO
Horizon $[H]$	64	64
Number of environments $[N_{\text{env}}]$	512	512
Actor learning rate $[\eta_a]$	1.64×10^{-3}	1.51×10^{-3}
Final learning rate $[\eta_{\text{final}}]$	5×10^{-4}	—
LR decay ratio $[\rho_{\text{lr}}]$	0.186	—
Weight decay $[w_d]$	0.01	—
Max gradient norm $[g_{\text{max}}]$	5.0	1/1
Discount $[\gamma]$	1	0.99
Critic learning rate $[\eta_c]$	—	1×10^{-3}
Epochs per update $[K]$	—	1
Minibatches $[N_{\text{mb}}]$	—	8
GAE $[\lambda_{\text{GAE}}]$	—	0.95
PPO clip $[\epsilon]$	—	0.2
Value loss weight $[c_v]$	—	0.5
Entropy weight $[c_{\text{ent}}]$	—	0.01

Results were averaged across $N_{\text{seed}} = 10$ unique random seeds. For each seed, the policy was retrained from scratch. We set the control timestep and maximum episode length to be $\Delta t_{\text{ctrl}} = 0.02$ s and $T_{\text{ep}} = 600$ respectively (total episode duration is 12 s). These parameters were selected to provide sufficient time for interception under the present configuration while keeping episodes short enough for efficient training and stable policy optimization. The capture radius was set to $c_r = 0.3$ m, corresponding approximately to the physical extent of a large intruder vehicle.

Observations and actions are expressed in the start frame, defined by the agent orientation at initialization rather than the global world frame. Anchoring commands to this frame removes dependence on a fixed global coordinate frame, allowing the learned policy to behave consistently regardless of the interceptor’s initial orientation.

Table 3 lists the algorithm-specific hyperparameters for APG and PPO side by side, with dashes indicating entries that are not applicable to a given method.

Table 4 specifies the intruder trajectory randomization applied at the start of each episode. Each parameter is sampled uniformly over the range shown in the table.

Finally, Tables 5 and 6 report the parameters for the two dynamics models used throughout the experiments. For the point mass dynamics (PMD) model, we identify the subset of parameters subjected to domain randomization during training to improve transferability to nonlinear quadrotor dynamics evaluation. The nonlinear quadrotor dynamics model parameters include the low-level controller parameters used to track policy outputs. For the algorithm benchmark, the modeled quadrotor mass during evaluation was set to 2.65 kg. For the APG dynamics comparison, the mass was reduced to 1.0 kg to increase the thrust-to-weight ratio, thereby simulating a more agile interceptor capable of handling higher-speed intruders.

Table 4: Intruder trajectory randomization during training. The speed range depends on benchmark: $\mathcal{U}(-4, 4)$ m/s for Figure 5 and $\mathcal{U}(-10, 10)$ m/s for Figure 7.

Parameter	Value
Speed [v_{tgt}] (m/s)	$\mathcal{U}(-10, 10) / \mathcal{U}(-4, 4)$
Tilt rpy [θ_{ilt}] (rad)	$\mathcal{U}(-0.5, 0.5)$
Axis radius [r_{axis}] (m)	$\mathcal{U}(4, 8)$
Aspect ratio [ρ_{ar}]	$\mathcal{U}(0.5, 1.5)$
Curve type	ellipse

Table 5: Point mass dynamics parameters with domain-randomization ranges.

PMD	Value
Sim. timestep [Δt_{sim}] (s)	0.0025
Control timestep [Δt_{ctrl}] (s)	0.02
Gravity [g] (m/s^2)	9.807
Quadratic drag [$k_{d,1}$]	0.1
Linear drag [$k_{d,2}$]	0.1
Accel. smooth factor [β_a]	12.0
Accel. smooth window [τ_a] (s)	1.0
Accel. ctrl delay [δ_a] (s)	0.02
Yaw smooth factor [β_ψ]	12.0
Yaw smooth window [τ_ψ] (s)	1.0
Yaw ctrl delay [δ_ψ] (s)	0.02
Vel. smooth factor [β_v]	0.5
Vel. smooth window [τ_v] (s)	2.0
<i>Domain randomization</i>	
Accel. smooth factor [β_a]	$\mathcal{U}(5, 12)$
Accel. ctrl delay [δ_a] (s)	$\mathcal{U}(0.01, 0.04)$
Yaw smooth factor [β_ψ]	$\mathcal{U}(5, 12)$
Yaw ctrl delay [δ_ψ] (s)	$\mathcal{U}(0.01, 0.05)$

Table 6: Nonlinear quadrotor dynamics parameters.

Quadrotor	Value
Sim. timestep [Δt_{sim}] (s)	0.0025
Control timestep [Δt_{ctrl}] (s)	0.02
Mass* [m] (kg)	2.65 / 1.0
Gravity [g] (m/s^2)	9.807
Quadratic drag [$k_{d,1}$]	0.1
Linear drag [$k_{d,2}$]	0.1
I_{xx}, I_{yy}, I_{zz} (kg m^2)	0.0143, 0.0175, 0.021
I_{xy}, I_{yz}, I_{xz} (kg m^2)	$2.9139 \times 10^{-7}, -4.25 \times 10^{-5}, -1.91 \times 10^{-5}$
Arm length [ℓ_{arm}] (m)	0.15
Moment scale [k_{moment}]	0.0108
Motor spread angle [θ_m] (rad)	0.7854
Rotor time constant [τ_r] (s)	0.0186
RPM range [$\Omega_{\text{min}}, \Omega_{\text{max}}$] (rev/s)	[2970, 20965]
<i>Low-level controller</i>	
PD pos. gain (x,y,z)	6.25, 6.25, 16.0
PD vel. gain (x,y,z)	5.0, 5.0, 8.0
PD rot. gain (x,y,z)	110, 89, 70
PD ang. vel gain (x,y,z)	20, 15, 15

*2.65 kg for Figure 5; 1.0 kg for Figure 7